The Astrophysical Journal, 897:146 (12pp), 2020 July 10 https://doi.org/10.3847/1538-4357/ab982b

The Multiwavelength Counterparts of Fast Radio Bursts

Ge Chen, Vikram Ravi, and Wenbin Lu
Cahill Center for Astronomy and Astrophysics, MC 249-17 California Institute of Technology, Pasadena CA 91125, USA; gcchen@caltech.edu
Received 2020 April 22; revised 2020 May 28; accepted 2020 May 30; published 2020 July 13

Abstract

The engines that produce extragalactic fast radio bursts (FRBs), and the mechanism by which the emission is generated, remain unknown. Many FRB models predict prompt multiwavelength counterparts, which can be used to refine our knowledge of these fundamentals of the FRB phenomenon. However, several previous targeted searches for prompt FRB counterparts have yielded no detections and have additionally not reached sufficient sensitivity with respect to the predictions. In this work, we demonstrate a technique to estimate the ratio, η, between the energy outputs of FRB counterparts at various wavelengths and the radio-wavelength emission. Our technique combines the fluence distribution of the FRB population with results from several wide-field blind surveys for fast transients from the optical to the TeV bands. We present constraints on η that improve upon previous observations even in the case where all unclassified transient events in existing surveys are FRB counterparts. In some scenarios for the FRB engine and emission mechanism, we find that FRB counterparts should have already been detected, thus demonstrating that our technique can successfully test predictions for η. However, it is possible that FRB counterparts are lurking among catalogs of unclassified transient events. Although our technique is robust to the present uncertainty in the FRB fluence distribution, its ultimate application to accurately estimate or bound η will require the careful analysis of all candidate fast transient events in multiwavelength survey data sets.

Unified Astronomy Thesaurus concepts: Radio bursts (1339); Radio transient sources (2008); Neutron stars (1108)

1. Introduction

Fast radio bursts (FRBs) are short (∼ms) and luminous ($\sim 10^{42}$ erg s^{-1}) radio pulses detected at extragalactic distances. There have been nearly a hundred FRBs reported (Petroff et al. 2016), and the estimated rate is $\sim 10^3$ sky^{-1} day^{-1} (Bhandari et al. 2018). Five FRB sources have been directly associated with host galaxies, revealing a range of galaxy classes and source environments (Chatterjee et al. 2017; Bannister et al. 2019; Prochaska et al. 2019; Ravi et al. 2019; Marcote et al. 2020). Repeat bursts have been observed from 20 FRB sources (Spitler et al. 2016; CHIME/FRB Collaboration et al. 2019a, 2019b; Kumar et al. 2019; Fonseca et al. 2020), indicating that at least some FRBs originate from noncatastrophic events (see also Ravi 2019). The exact FRB emission mechanism(s) and engine(s) remain elusive.

The high brightness temperatures ($\sim 10^{35}$ K) of FRBs require a coherent emission process. Although several astrophysical coherent emission mechanisms are identified with Galactic sources (Melrose 2017), these mechanisms encounter difficulties with the energy scales of FRBs. Two classes of mechanisms have been proposed for FRBs (although see, e.g., Lyubarsky 2020): synchrotron masers (e.g., Lyubarsky 2014; Beloborodov 2017; Ghisellini 2017; Waxman 2017; Metzger et al. 2019) and coherent curvature radiation (e.g., Cordes & Wasserman 2016; Kumar et al. 2017). Synchrotron masers require a population inversion in the emitting lepton energy and pitch-angle distribution. This is generally thought to be possible in an ultrarelativistic (bulk Lorentz factor $\Gamma \gg 1$) radiative shock driven into a significantly magnetized plasma (magnetization parameter $\sigma \gtrsim 10^{-3}$); the shock is mediated by Larmor-rotating charges, which results in the population inversion within the shock. The curvature-radiation mechanism instead scales ideas for the generation of pulsar radio emission to FRB energy scales, invoking coherently radiating bunches of relativistic ($\Gamma \sim 30$) leptons accelerated by magnetic reconnection events. These radiation processes are discussed in the context of several progenitor models. The majority of these models involve highly magnetized neutron stars/magnetars, because the short durations and high luminosities of FRBs require compact, active engines with large energy budgets and emission-region field strengths of $\gtrsim 10^{10}$ G.

Several classes of FRB models (emission mechanism and/or engine) predict prompt multiwavelength counterparts and specify the ratio between the energy emitted by the counterpart and by the FRB. Synchrotron masers initiated by ultrarelativistic shocks are accompanied by synchrotron emission from fast-cooling shock-heated electrons that cascade through the γ-ray and X-ray bands on subsecond timescales, or perhaps through the optical/near-infrared (NIR) bands in the case of an electron–positron plasma upstream of the shock (Metzger et al. 2019). Specific luminosities comparable to or greater than the FRB luminosities are predicted for the higher-energy emission. Additionally, although the curvature-radiation mechanism does not naturally produce multiwavelength emission, the mechanism may be triggered by events that do radiate across the electromagnetic spectrum (e.g., the cosmic comb model; Zhang 2017).

We define the ratio between the energy radiated by an FRB event in a given electromagnetic band and in the radio band as

$$\eta(\nu_c) = \frac{F_{\rm Band}}{F_{\rm Radio}} \approx \frac{\nu_{\rm 1,Band} \cdot F_{\nu,\rm Band}}{\nu_{\rm 1,Radio} \cdot F_{\nu \rm Radio}}. \quad (1)$$

Here, ν_c is the central frequency of the band of interest, $F_{\rm Radio}$ and $F_{\rm Band}$ are the band-integrated fluences in the band of interest and the radio band, respectively, $F_{\nu,\rm Radio}$ and $F_{\nu,\rm Band}$ are the specific fluences, and $\nu_{\rm 1,Band}$ and $\nu_{\rm 1,Radio}$ are the lower-frequency bounds of these two bands. The commonly made approximation in the second step (Gehrels 1997) assumes that

the bands span natural-logarithmic frequency intervals, but is accurate in general when the specific fluence scales as $F_\nu \propto \nu^{-2}$ and the band upper-frequency bound ν_2 is much greater than the lower bound ν_1. We also define a fluence ratio as

$$\eta_\nu(\nu_c) = \frac{F_{\nu,\mathrm{Band}}}{F_{\nu,\mathrm{Radio}}}. \quad (2)$$

In this work, we consider how constraints on η and η_ν based on the possible detection, or nondetection, of multiwavelength FRB counterparts can test FRB models.

Until 2019 December, no FRB multiwavelength counterpart has been confirmed. Most previous observational constraints on η are derived from searches for multiwavelength transient emissions that are close to the FRBs in both time and location (see Section 5.2 for references). It is also possible to search for multiwavelength transient events that are close to the FRBs in location only, but at any time.

In this work, we explore a third method: a blind search of the whole sky for unclassified multiwavelength transient events at any time. Several surveys across the optical and high-energy bands explore the sky with subsecond time resolution. We develop and demonstrate a method to estimate η by combining relevant multiwavelength survey parameters with the fluence distribution of the currently observed FRB population. This method can only directly constrain η when the statistics of unclassified short-duration transient events are published. However, these statistics are rarely published. We therefore compare constraints derived assuming no multiwavelength FRB counterparts have been detected with predictions from FRB emission models. We find in several scenarios that existing surveys are likely/unlikely to have already detected FRB counterparts. For some surveys, we also consider the case where a fraction of their unclassified events are indeed FRB counterparts to derive upper bounds on η.

We propose our method for three reasons. First, a blind search for counterparts is meaningful because some models predict cases where the radio emission from an FRB is undetectable while the counterpart is. For example, Metzger et al. (2019) show that high-energy counterpart emission may escape a dense medium surrounding the source even when the radio emission is subject to the obscuring effects of scattering and absorption. Second, it is reasonable to make use of the statistical properties of FRBs. The estimated FRB rate above $F_{\nu,0} \sim 2$ Jy ms is $R_0 \approx 1.7 \times 10^3$ sky^{-1} day^{-1} (Bhandari et al. 2018), sufficiently large to be treated as a common event for relatively large telescopes scanning across most of the sky in a blind survey (Vedantham et al. 2016). Third, we will show that our technique provides stronger constraints than previous multiwavelength observations in the current situation wherein no counterpart has been detected.

We explain the method to estimate the band-to-radio energy ratio η in Section 2, introduce the surveys under consideration in Section 3, and show our calculations and results in Section 4. In Section 5, we compare our results with theoretical predictions made by leading FRB emission models. We also compare our results with previous observational constraints and discuss observational strategies for future blind searching. We conclude in Section 6.

2. Methods

We adopt the broken-power-law specific-fluence cumulative distribution function (CDF) estimated using the Australian Square Kilometre Array Pathfinder (ASKAP) and Parkes FRB samples (James et al. 2019):

$$R(F_\nu) = \int_F^\infty r(F'_\nu) dF'_\nu, \quad (3a)$$

$$= R_0 \left(\frac{F_\nu}{F_{\nu,0}}\right)^{\alpha_1} \quad (F_{\nu,\min} < F_\nu < F_{\nu,b}), \quad (3b)$$

$$= R_b \left(\frac{F_\nu}{F_{\nu,b}}\right)^{\alpha_2} \quad (F_\nu > F_{\nu,b}). \quad (3c)$$

Here, $R(F_\nu)$ is the FRB rate (in the usual units of sky^{-1} day^{-1}) above a given fluence threshold F_ν in the radio band, $r(F_\nu)$ is the differential fluence distribution function, $\alpha_1 = -1.18$, $\alpha_2 = -2.2$, $F_{\nu,\min}$ is the (observationally unconstrained) fluence cutoff in the radio band, $F_{\nu,0} \sim 2$ Jy ms is the fluence completeness threshold for the Parkes FRB searches (Keane & Petroff 2015), $R_0 \approx 1.7 \times 10^3$ sky^{-1} day^{-1} is the estimated rate above $F_{\nu,0}$ (Bhandari et al. 2018), $F_{\nu,b}$ is the fluence break which we choose to be 15 Jy ms, and $R_b \approx 171$ sky^{-1} day^{-1} is the rate above F_b calculated from Equation (3(b)).

We assume that in any other emission band the fluence CDF, $\tilde{R}$, has the same functional form as R, except with a shift in abscissa (i.e., horizontally) and a renormalization:

$$\tilde{R}(F_\nu) = R\left(\frac{F_\nu}{\eta_\nu}\right). \quad (4)$$

We use properties of multiwavelength surveys to estimate η_ν by calculating the degree to which the distribution needs to be shifted in its abscissa to achieve the same detection rate in two different bands.

We now describe how estimates of η and η_ν are made. Suppose that a transient survey has a field of view (FOV) of Ω steradians, effectively lasts for n days, and has not detected any FRB counterpart. The survey operates at frequencies from ν_1 to ν_2, with a center frequency of ν_c. Our method involves the following steps:

1. Convert the instrumental detection sensitivity threshold to an energy flux, f_0.
   (a) If the photon flux threshold f_{ph} is specified, we calculate f_0 using the specifications of each instrument and the weighted average photon frequency $\langle\nu\rangle$ in this band, assuming a typical photon index of -2 (i.e., a spectral index of -1; see, e.g., Atwood et al. 2009)[1]:

$$f_0 = f_{\mathrm{ph}} \cdot h\langle\nu\rangle,$$
$$= f_{\mathrm{ph}} \cdot h \frac{\int_{\nu_1}^{\nu_2} d\nu\, \nu^{-2}\, \nu}{\int_{\nu_1}^{\nu_2} d\nu\, \nu^{-2}},$$
$$= f_{\mathrm{ph}} \cdot h \frac{ln(\nu_2/\nu_1)}{\nu_1^{-1} - \nu_2^{-1}}. \quad (5)$$

[1] This assumption yields larger estimates for η than if a steeper photon index were assumed (see Section 4). Some previous studies (e.g., Tendulkar et al. 2016) assume steeper photon indices.

(b) If we know the limiting magnitude m,

$$f_0 = 10^{-0.4m} \cdot \nu_1 \cdot f_{\nu,\mathrm{m0}}. \quad (6)$$

Here, $f_{\nu,\mathrm{m0}}$ is the specific energy flux of an object with zero magnitude in that band and magnitude system (Frei & Gunn 1994; Fukugita et al. 1996; Bessell et al. 1998).

2. Scale the detection limiting energy flux f_0 according to a timescale Δt. Specifically, if the survey has an automatic self-trigger algorithm for burst candidates, we use the trigger timescale(s) t_{trig}. Otherwise, we use the nominal instrumental time resolution t_{res}. Because the signal-to-noise ratio $\mathrm{S/N} \propto \Delta t^{1/2}$, the detection flux threshold $f_0 \propto \Delta t^{-1/2}$. (Note that if the burst duration $t_{\mathrm{burst}} < \Delta t$, the corresponding intrinsic burst flux needs to be higher than f_0. Otherwise, they are the same.)
3. Compute the fluence thresholds of the burst in the band of interest.
   (a) If $t_{\mathrm{burst}} < \Delta t$, the band-integrated burst fluence limit is $F_{0,\mathrm{Band}} = f_0 \cdot \Delta t$.
   (b) Otherwise, Δt is too short for the burst. One should either choose a different timescale or bin-adjacent time samples.

The specific-fluence threshold is $F_{\nu,0,\mathrm{Band}} \approx F_{0,\mathrm{Band}}/\nu_1$. In addition, we require that the number of photons received within the timescale (Δt) by the telescope's effective collecting area (A) is at least one. When this is not satisfied, we replace the photon flux threshold f_{ph} (step 1) with 1 photon $\Delta t^{-1} A^{-1}$ and repeat the previous steps.

4. Calculate the event-rate upper bound in this survey if no candidate was detected:

$$R(F_{\nu,0,\mathrm{Band}}) \leqslant \frac{3}{n}\frac{4\pi}{\Omega}\ \mathrm{sky}^{-1}\,\mathrm{day}^{-1}. \quad (7)$$

A nondetection means a Poisson single-sided upper limit of 3 at the 95% confidence level (Gehrels 1986). Alternatively, if there were x candidate events in this survey, the event rate would be

$$R = \frac{x}{n}\frac{4\pi}{\Omega}\ \mathrm{sky}^{-1}\,\mathrm{day}^{-1}. \quad (8)$$

5. Solve for the radio-band fluence threshold $F_{\nu,0,\mathrm{Radio}}$ that would have produced the same rate R using Equation (3).
6. Find the fluence ratios:

$$\eta_\nu(\nu_c) \leqslant F_{\nu,0,\mathrm{Band}}/F_{\nu,0,\mathrm{Radio}} \quad (9)$$

and

$$\eta(\nu_c) \leqslant F_{0,\mathrm{Band}}/F_{0,\mathrm{Radio}} \approx \frac{F_{0,\mathrm{Band}}/\nu_{1,\mathrm{Band}}}{F_{0,\mathrm{Radio}}/\nu_{1,\mathrm{Radio}}}. \quad (10)$$

Here, $F_{\nu,0,\mathrm{Band}}$ and $F_{\nu,0,\mathrm{Radio}}$ have been found in steps 3 and 5, respectively.

3. Existing Surveys

We demonstrate the application of the methods outlined above using existing high-time-resolution transient surveys from the NIR band up to the TeV band. Following model predictions (see Section 5), we assume that FRB counterparts are fast transient events shorter than about a few minutes. In this work, we only focus on surveys with short cadences ($\lesssim$2 minutes), large FOVs, and relatively high sensitivities.

Table 1 lists the survey instruments considered in this work. The survey durations are counted until 2019 October 1. We assume full-time operation since the launch date for space missions and a typical average observation time of 8 hr per day since the operation date for ground-based instruments. We adopt the detection threshold used by each instrument, although some of them correspond to different statistical S/Ns, as each survey could have different false-positive rates. We list the threshold corresponding to the given timescale, unless specified otherwise. We increase the detection threshold of MAGIC and Fermi/LAT (at the lower timescale) to 2.4×10^{-11} and 7×10^{-8} photon cm^{-2} s^{-1}, respectively, to satisfy the requirement that at least one photon is received by the corresponding telescopes within the timescales (step 3).

The timescales are chosen differently for the high-energy and the optical bands. All of the high-energy surveys selected in this work have been designed to be sensitive to GRB-like transient events ($\sim$0.1 to $\sim$100 s). Each survey has its own transient-candidate self-trigger algorithm that runs on board commensally with observations using a range of trial trigger timescales. In addition, it is also possible to manually search the survey data afterwards for candidate events using different algorithms and timescales. For Fermi/LAT, we adopt the timescales optimized for FRB-counterpart searching (Cunningham et al. 2019), as the onboard trigger only responds to very bright bursts due to the high cosmic-ray rate.[2] For the other high-energy surveys, we list the trial timescales used by the corresponding self-trigger algorithms. In the optical band, we use the nominal time resolutions for all instruments.

4. Results

We estimate η for each survey/instrument (Table 1) following the steps introduced in Section 2. Table 2 and Figure 1 summarize the results. In Section 4.1, we make the assumption that no counterpart has been detected to demonstrate the power of our technique. In Section 4.2, we investigate the implications of assuming that counterparts exist among the unclassified transient events in some surveys.

4.1. Band-to-radio Fluence Ratios Assuming Nondetections

In Table 2, we list 95% confidence upper limits on the rate of FRB counterparts and on η for each survey. We use a reference frequency of $\nu_{1,\ \mathrm{Radio}} = 1.182$ GHz (the lower limit of the Parkes radio band) to convert the specific fluence into the band-integrated radio fluence (in step 6). We assume that the counterpart duration t_{burst} is shorter than the timescale Δt for all instruments (in step 3 above) and discuss the alternative case in Section 5. For surveys with multiple timescales, we scale the flux and fluence following steps (2) and (3) using the shortest and longest timescales. We list the corresponding results in two rows in Table 2 and plot both ratios in Figure 1(a).

Our results are robust within an order of magnitude to a selection of variations in the fluence distribution model in Equation (3) (Macquart & Ekers 2018). We vary the broken-power-law indices α_1 and α_2 by $\pm$0.7 and find that the results change by 46% ($\alpha_1 = -0.48$), 86% ($\alpha_1 = -1.88$), 92% ($\alpha_2 = -1.5$), and 270% ($\alpha_2 = -2.9$), respectively. We also use a single-power-law fluence distribution model with an

[2] N. Omodei (2020, personal communication).

Table 1
Existing Surveys and Instruments

Instrument	Band	Effective Duration (days)	Detection Threshold	Timescales	FOV
MAGIC[a]	50 GeV–50 TeV	613	7.6×10^{-12} photons cm^{-2} s^{-1}[b]	e.g., 10 ms	4.8 deg^2
Fermi/LAT[c]	20 MeV–300 GeV	4132	3×10^{-9} photons cm^{-2} s^{-1}[d]	0.1 s to 100 s	2.4 sr
Fermi/GBM[e]	8 keV–40 MeV	4132	0.74 photons cm^{-2} s^{-1}	16 ms to 8.192 s	>8 sr
CGRO/BATSE[f]	30 keV–1.9 MeV	3348	3×10^{-8} erg cm^{-2} s^{-1}	64 ms to 1.024 s	4π sr
SWIFT/BAT[g]	15–150 keV	5344	$\sim 10^{-8}$ erg cm^{-2} s^{-1}	4 ms to 32 s	1.4 sr
MAXI/GSC[h]	2–30 keV	3729	$\sim 7 \times 10^{-10}$ erg cm^{-2} s^{-1}	1 s to 30 s	$1.^\circ5 \times 160^\circ$
Gaia[i]	330–1050 nm	2112	$G = 20.6$ mag (Vega)	4.5 s	$0.^\circ85 \times 0.^\circ66$
PTF/iPTF[j]	≈400–700 nm	973	$R \approx 20.6$ (AB)	60 s	≈8 deg^2
Pi of the Sky[k]	≈320–900 nm	756	$V = 12$ mag (assume Vega)	10 s	6400 deg^2
MMT-9[l]	≈400–800 nm	644	$V = 11$ mag (assume Vega)	0.128 s	900 deg^2
Evryscope[m]	≈400–700 nm	533	$V = 16.4$ mag (assume Vega)	120 s	8660 deg^2

Notes.
[a] Aleksić et al. (2016). The Major Atmospheric Gamma Imaging Cerenkov telescopes (MAGIC) comprise two Imaging Atmospheric Cerenkov telescopes. One has been operating since 2005 April, the other since 2009 fall, and both were upgraded in 2012 summer. Here we calculate the duration from 2009 September and assume 4 hr of observation per day.
[b] The sensitivity corresponds to a 50 hr observation of a point source with Crab Nebula–like spectrum above 104 GeV. However, we increase the threshold to 2.4×10^{-11} photons cm^{-2} s^{-1} to satisfy the requirements that at least one photon is received within 10 ms by the MAGIC effective collecting area of 10^9 cm^2.
[c] Atwood et al. (2009) and https://fermi.gsfc.nasa.gov. The Fermi Gamma-Ray Space Telescope (FGST) was launched on 2008 June 11.
[d] The detection threshold corresponds to a one-year survey at high latitude and >100 MeV, assuming a source photon spectral index of −2. However, for the shortest timescale of 0.1 s, we increase the threshold to 7×10^{-8} photons cm^{-2} s^{-1} to satisfy the requirements that at least one photon is received within 0.1 s by the Fermi/LAT effective collecting area of 8000 cm^2.
[e] Meegan et al. (2009) and https://fermi.gsfc.nasa.gov. The threshold is for a pulse in the band of 50–300 keV and 1 s peak.
[f] https://heasarc.gsfc.nasa.gov/docs/cgro/cgro/. The Burst And Transient Source Experiment (BATSE) on the Compton Gamma Ray Observatory (CGRO) was in operation from 2000 April to 2009 June. The threshold was for a 1 s burst.
[g] Barthelmy et al. (2005). The BAT monitor archive begins on 2005 February 12. The threshold is for a ∼1 s peak.
[h] Matsuoka et al. (2009). MAXI was launched on 2009 July 16. The threshold corresponds to one International Space Station orbit, in which an object stays in the FOV for at least 45 s. For the timescales, we ignore those with ⩾1 scan as they are too long for a millisecond-scale transient.
[i] Prusti et al. (2016), https://www.cosmos.esa.int/web/gaia, and http://www.astro.utu.fi/~cflynn/galdyn/lecture10.html. The spacecraft was launched on 2013 December 19.
[j] Law et al. (2009). Operating from 2009 March to 2017 February.
[k] Mankiewicz et al. (2014) and Cwiek et al. (2014). The full system started to operate in 2013 July. Assume the Vega magnitude system.
[l] Biryukov et al. (2015), Mini-MegaTORTORA. The high time resolution started to operate in 2014 June. Assume the Vega magnitude system.
[m] Law et al. (2015). Evryscope-South started to operate in 2015 May. We do not include Evryscope-North necause it started operations in 2019. Assume the Vega magnitude system.

index of −1.5 and find that the results change by less than 88%. However, our results are sensitive to the choice of the photon index in the γ-ray band. In step 1, we assume a Crab-like photon index of 2 to calculate the energy flux limit from the photon flux limit for MAGIC, Fermi/LAT, and GBM. We vary the photon index to −2.5 and −1.5 and find that the resulting fluence ratios decrease/increase by 70% and one order-of-magnitude, respectively. There is little theoretical guidance on what range of photon indices is reasonable for FRB counterparts, but the example of GRBs suggests that photon indices > -2 are expected below peak energies (in νF_ν spectra) of typically 100 keV–1 MeV, and photon indices < -2 are expected above the peak energies (Preece et al. 1998).

4.2. What if FRB Counterparts Have Been Detected?

No compelling candidate FRB counterpart at any wavelength had been reported until the end of 2019. However, we cannot exclude the possibility that some unclassified short transient events found in existing surveys could be associated with FRBs. It is beyond the scope of this paper to estimate what fraction of them might be FRB counterparts, but we will investigate the results assuming the extreme case where all of them are FRB counterparts. We show the results in Table 2 (within parentheses) and Figure 1(b) (dashed lines).

In the Fermi/GBM trigger catalog[3] to the end of 2019, there were 7045 triggered events, and 370 of them were marked as "uncertain classification." We discuss two limiting cases for these unclassified short transient events. First, if none of them were FRB counterparts, the results would be the same as those of Section 4.1. Second, if all of them were FRB counterparts, we estimate η using the method in Section 2. Using the shortest trigger timescale as an example, steps 1 to 3 remain the same, so the Fermi/GBM fluence limit is still 1.02×10^{18} Jy ms Hz. In step 4, the rate is now estimated to be $R = \frac{370}{4132 \text{ days}} \frac{4\pi \text{ sky}^{-1}}{8} = 0.14 \text{ day}^{-1} \text{ sky}^{-1}$, ∼100 times larger than the upper limit assuming nondetection. In the radio band, the fluence threshold that would have produced the new detection rate is 380 Jy ms, or 4.49×10^{11} Jy ms Hz. Hence, $\eta = \frac{1.02 \times 10^{18}}{4.49 \times 10^{11}} \approx 2.27 \times 10^6$, ∼10 times higher than our result in Section 4.1.

In the MAXI trigger catalog[4] between 2011 April 18 and 2020 January 28, 168 events were classified as "either GRB or unknown X-ray transient." If all of them were FRB counterparts, the rate would be $R = \frac{168}{3207 \text{ days}} \frac{4\pi \text{ sky}^{-1}}{0.0731} = 9.00 \text{ day}^{-1} \text{ sky}^{-1}$. The

[3] https://heasarc.gsfc.nasa.gov/db-perl/W3Browse/w3hdprods.pl
[4] https://gcn.gsfc.nasa.gov/maxi_grbs.html

Table 2
Results

Instrument	ν_c (Hz)	Flux Threshold f_0 (erg cm^{-2} s^{-1})	Fluence Threshold F_0 (Jy ms Hz)	Rate[a] (sky^{-1} day^{-1})	η_ν	η[a]
MAGIC	6.05×10^{27}	5.54×10^{-8}	5.54×10^{16}	42	1.61×10^{-10}	1.65×10^{6}
Fermi/LAT	3.63×10^{25}	3.85×10^{-7}	3.85×10^{18}	3.80×10^{-3}	4.07×10^{-7}	1.67×10^{6}
		5.19×10^{-10}	5.19×10^{18}		5.49×10^{-7}	2.25×10^{6}
Fermi/GBM	4.84×10^{21}	6.39×10^{-7}	1.02×10^{18}	1.14×10^{-3} (0.14)	1.56×10^{-4}	2.56×10^{5} (2.27×10^{6})
		2.82×10^{-8}	2.31×10^{19}		3.54×10^{-3}	5.79×10^{6} (5.15×10^{7})
CGRO/BATSE	2.33×10^{20}	1.19×10^{-7}	7.59×10^{17}	8.96×10^{-4}	2.77×10^{-5}	1.70×10^{5}
		2.96×10^{-8}	3.04×10^{18}		1.11×10^{-4}	6.81×10^{5}
Swift/BAT	1.99×10^{19}	1.58×10^{-7}	6.32×10^{16}	5.04×10^{-3}	1.01×10^{-5}	3.11×10^{4}
		1.77×10^{-9}	5.66×10^{18}		9.07×10^{-4}	2.78×10^{6}
MAXI/GSC	3.87×10^{18}	4.70×10^{-9}	4.70×10^{17}	1.38×10^{-1} (9.00)	2.54×10^{-3}	1.04×10^{6} (6.95×10^{6})
		7.00×10^{-10}	2.10×10^{18}		1.14×10^{-2}	4.65×10^{6} (3.11×10^{7})
Gaia	5.97×10^{14}	6.13×10^{-14}	2.76×10^{13}	1.04×10^{2}	5.15×10^{-3}	1.24×10^{3}
PTF/iPTF	5.89×10^{14}	7.92×10^{-14}	4.77×10^{14}	15.9	2.52×10^{-2}	9.13×10^{3}
Pi of the Sky	6.35×10^{14}	2.00×10^{-10}	2.00×10^{17}	2.56×10^{-2}	7.30×10^{-1}	1.06×10^{5}
MMT-9	5.62×10^{14}	5.65×10^{-10}	7.23×10^{15}	2.13×10^{-1}	6.16×10^{-2}	1.95×10^{4}
Evryscope	5.89×10^{14}	4.47×10^{-12}	5.36×10^{16}	2.68×10^{-2}	1.55×10^{-1}	5.63×10^{4}

Note.
[a] Rate and η results outside parentheses assume no FRB-counterpart detection (Section 4.1), and are to be interpreted as 95% confidence upper limits. Results in parentheses assume that all unclassified short transients were FRB counterparts (Section 4.2) and are thus to be interpreted as nominal upper limits.

radio fluence that could have produced the same rate would be 6.76×10^{10} Jy ms Hz, and the fluence ratio would be $\eta = \frac{4.70 \times 10^{17}}{6.76 \times 10^{10}} \approx 6.95 \times 10^{6}$, ~7 times higher than our previous result.

In the optical band, we only use the most constraining result (from Gaia) in the following comparison with model predictions and previous observations. No unclassified fast Gaia transient has been reported,[5] and so we tentatively maintain the nondetection assumption for Gaia in our results. This may change as more Gaia data are searched for unclassified fast transients.

5. Discussion

We have developed and demonstrated a technique to estimate the ratios between FRB energy output in the radio band and in various bands from the near-IR to γ-rays. Preliminary results based on published surveys for fast transients (Table 1) are presented in Table 2 and Figure 1 in two extreme cases: assuming either that no FRB counterpart has been detected or assuming that all unclassified fast transients are FRB counterparts. Our method uses the statistical properties of the observed FRB population, while most of the previous observational estimations are based on multiwavelength observations at the locations of individual FRB events. In this section, we will compare our results with theoretical predictions and previous observations, and briefly discuss possible future FRB-counterpart search strategies.

5.1. Comparison to Theoretical Predictions

The two leading FRB emission mechanisms are the synchrotron maser and coherent curvature radiation. We first compare our high-energy results with predictions from these two types of models, as well as a class of models generally involving contemporaneous high-energy flares, and the cosmic comb model. We then compare our optical results with model predictions made under five scenarios. Finally, we conclude by calculating the model-predicted counterpart detection rate for some of the existing surveys (Table 3). This section is partly intended as a pedagogical resource for future studies of FRB multiwavelength counterparts.

5.1.1. Metzger et al. (2019) Model

Synchrotron masers have been widely discussed as an astrophysical coherent emission process (e.g., Hoshino & Arons 1991; Long & Pe'er 2018), and one common variation is coherent emission from synchrotron masers produced by ultrarelativistic shock in magnetized plasmas (e.g., Langdon et al. 1988; Lyubarsky 2014; Beloborodov 2017, 2019; Margalit et al. 2020; Metzger et al. 2019). Metzger et al. (2019) describe a model using particle-in-cell (PIC) simulation results for maser emission and the dynamics of self-similar shock deceleration. Magnetar flares eject supersonic ultrarelativistic ion–electron shells into the surrounding magnetized transrelativistic ion–electron plasma released by previous flares. The forward shock creates a population inversion and enables the synchrotron-maser process, which results in a narrowly peaked coherent radio emission putatively responsible for FRBs. The same forward shock, however, primarily dissipates energy through a synchrotron "afterglow" that will result in observable high-energy counterparts. The model predicts that the observed counterpart luminosity is $L_\gamma \sim 10^{45}$–10^{46} erg s^{-1}, with a duration of ~0.1–10 ms in the MeV–GeV band, and $L_X \sim 10^{42}$–10^{53} erg s^{-1}, with a duration of ~0.1–1 s in the keV band. A weak optical counterpart is possible if the upstream plasma were composed of electrons and positrons rather than electrons and ions; we do not consider any resulting quantitative predictions here. We convert the above predictions to fluence ratios η, which can be

[5] Wevers et al. (2018) developed a method to search the Gaia data for fast transients between tens of seconds to hours. They find four events produced by stellar flares in 23.5 deg^2 of sky.

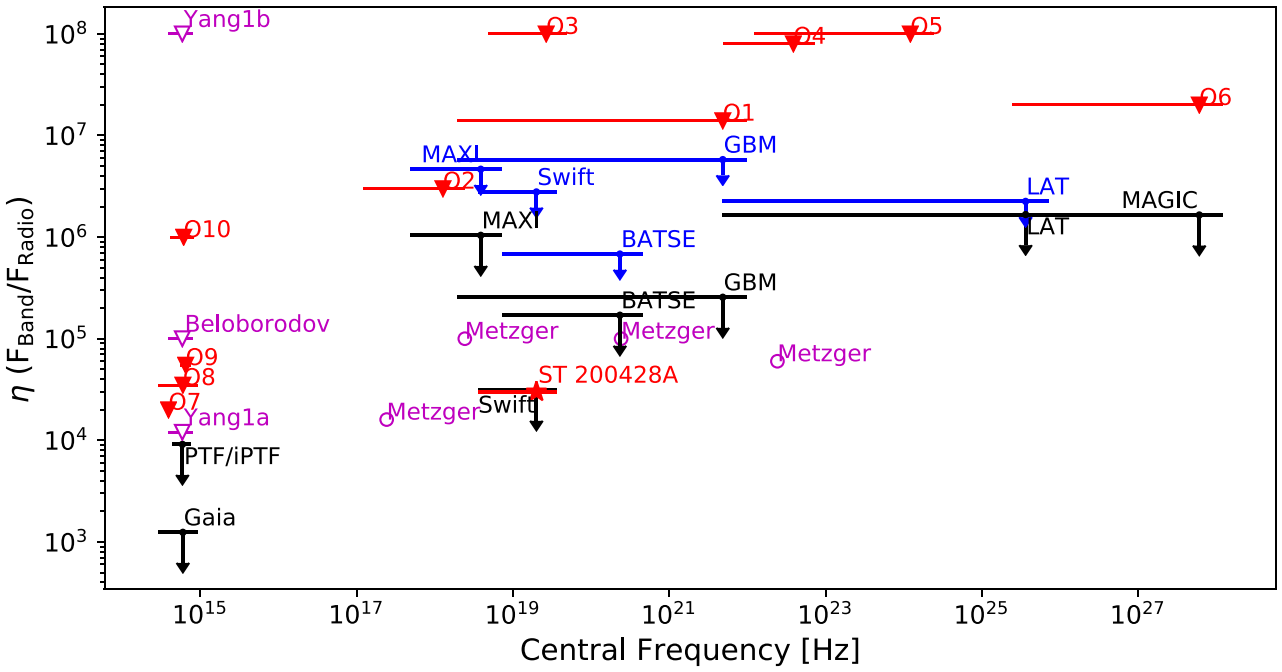

(a)

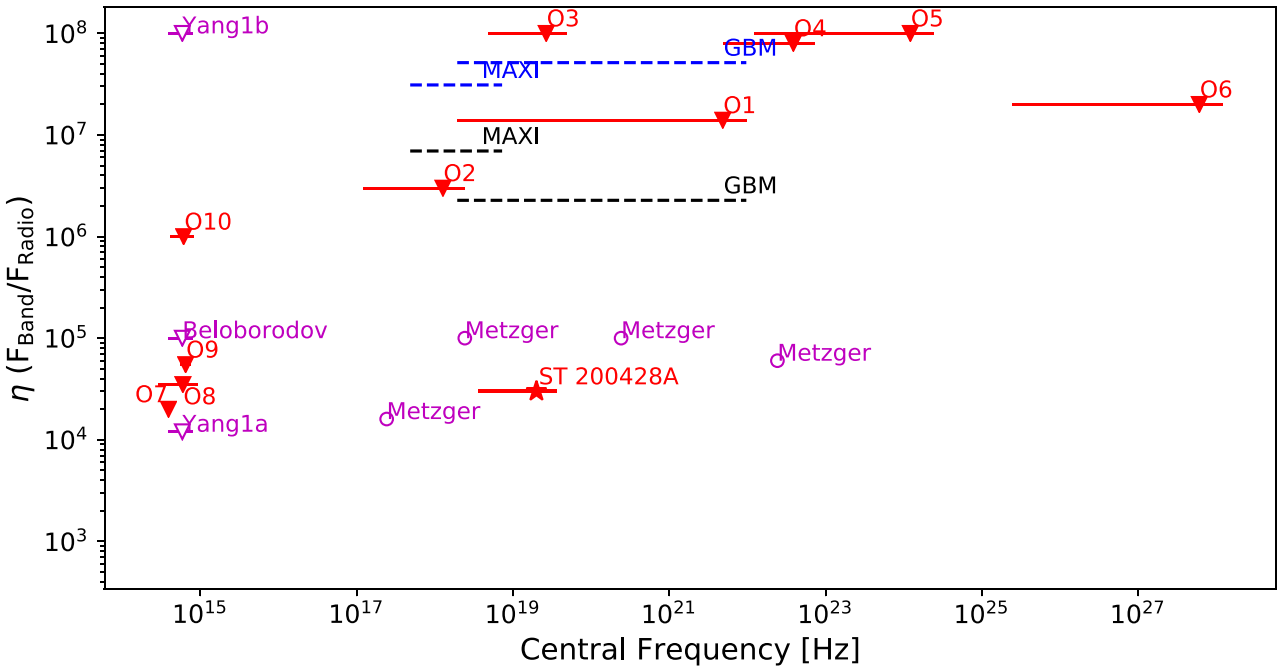

(b)

Figure 1. Constraints on the band-integrated fluence ratios from our results using the shortest and the longest timescales (black and blue lines, respectively; see Section 4), previous model predictions (the unfilled magenta markers are circles for predicted values and triangles for predicted upper limits; see Section 5.1), and previous observations (filled red star and triangles; "O1" to "O10" each represents the upper limit from Scholz ("O1" and "O2"), Anumurlapudi, Yamasaki, Casentini, MAGIC Collaboration, Hardy, Wevers, Andreoni and Richmond, respectively; see Section 5.2). (a) Our 95% confidence upper limits assuming nondetection using the shortest timescales (solid black lines) and the longest timescales (solid blue lines). (b) Our nominal upper limits assuming that all of the unclassified events in the trigger catalogs were FRB counterparts, using the shortest (dashed black lines) and the longest (dashed blue lines) timescales.

directly compared with our results. Assuming a typical FRB of duration 1 ms initiated by a flare of energy $\sim 10^{44}$ erg, the results of Metzger et al. (2019) imply ratios of 6×10^4, 10^5, 10^5, and 2×10^4 for a counterpart whose band starts from 100 MeV, 1 MeV, 10 keV, and 1 keV, respectively (hollow magenta circles in Figure 1).

Table 3
Theoretical Predictions and Expected Counterpart Rate

Model	Band	$t_{\rm Counterpart}$	η_ν	η	Instrument	Timescale[a]	Rate ($\rm sky^{-1}\ day^{-1}$)	$\langle n\rangle$[b] (days)	Survey Duration[c] (days)
Metzger	$\nu_1 = 100$ MeV	~3 ms	$\sim 2.8\times10^{-9}$	$\sim 6.0\times10^{4}$	Fermi/LAT	0.1 s	2.29×10^{-6}	2.29×10^{6}	4132
Metzger	$\nu_1 = 1$ MeV	~50 ms	$\sim 4.1\times10^{-7}$	$\sim 10^{5}$	Fermi/GBM	64 ms	2.13×10^{-5}	7.36×10^{4}	4132
					CGRO/BATSE	64 ms	1.89×10^{-4}	5.30×10^{3}	3348
Metzger	$\nu_1 = 100$ keV[d]	~1 s	$\sim 4.1\times10^{-6}$	$\sim 10^{5}$	Swift/ BAT	1.024 s	10^{-4}	8.95×10^{4}	5344
					CGRO/BATSE	1.024 s	8.94×10^{-6}	1.12×10^{5}	3348
Metzger	$\nu_1 = 10$ keV	~1 s	$\sim 4.1\times10^{-5}$	$\sim 10^{5}$	Fermi/GBM	1.024 s	1.01×10^{-6}	1.55×10^{6}	4132
Beloborodov	Optical	~1 s	$\lesssim 2.0\times10^{-1}$	$\lesssim 10^{5}$	Gaia	4.5 s	$\lesssim 6.31\times10^{5}$	$\gtrsim 1.17\times10^{-1}$	2112
Yang 1a[e]	Optical	~1 ms	$\lesssim 2.0\times10^{-2}$	$\lesssim 1.2\times10^{4}$	Gaia	4.5 s	$\lesssim 3.98\times10^{3}$	$\gtrsim 18$	2112
			$\gtrsim 1.7\times10^{-13}$	$\gtrsim 1.2\times10^{-7}$	Gaia	4.5 s	$\gtrsim 1.76\times10^{-21}$	$\lesssim 4.18\times10^{25}$	
Yang 1b	Optical	~a few × 10 s	$\lesssim 1.7\times10^{2}$	$\lesssim 10^{8}$	Gaia	≈45 s	$\lesssim 1.40\times10^{11}$	$\gtrsim 5.27\times10^{-7}$	2112
Yang 1c	Optical	~1 ms	$\lesssim 6.6\times10^{-7}$	$\lesssim 3.8\times10^{-1}$	Gaia	4.5 s	$\lesssim 5.51\times10^{-7}$	$\gtrsim 1.34\times10^{11}$	2112
Yang 2a	Optical	~1 ms	$\lesssim 6.6\times10^{-11}$	$\lesssim 3.8\times10^{-5}$	Gaia	4.5 s	$\lesssim 8.73\times10^{-16}$	$\gtrsim 8.43\times10^{19}$	2112
Yang 2b	Optical	~1 ms	$\lesssim 6.6\times10^{-10}$	$\lesssim 3.8\times10^{-4}$	Gaia	4.5 s	$\lesssim 1.38\times10^{-13}$	$\gtrsim 5.32\times10^{17}$	2112

Notes.
[a] The shortest instrumental timescale above the theoretical counterpart duration.
[b] The expected number of days to detect one single counterpart using the corresponding instrument (Poisson errors ignored).
[c] Same as the effective duration in Table 1.
[d] η interpolated between 1 MeV and 10 keV.
[e] E.g., "1a" refers to case 1, scenario (a) in the model (Section 5.1).

5.1.2. Beloborodov (2019) Model

Meanwhile, Beloborodov (2019) proposes that the synchrotron maser is formed instead when the magnetar giant flares launch ultrarelativistic blast waves ($\Gamma \gtrsim 10^3$) into the relativistic ($\Gamma \sim 10^2$), persistent magnetar wind outflow, which consists of $e^{\pm}$. A bright optical counterpart occurs only when the blast wave strikes a hot wind bubble in the slow ion tail of a previous flare. The optical flash is estimated to have a duration of ~1 s and an energy upper limit of $\sim 10^{44}$ erg. The optical-to-radio fluence ratio would be $\eta \lesssim 10^5$ using the average FRB 121102 burst energy of 10^{39} erg (Law et al. 2017) and $\eta \sim 10^3$ using the FRB energy corresponding to the strongest explosion, which produces the brightest optical flash in their model. The former is shown in Figure 1 to compare with our results, as our technique utilizes the statistical features of the entire FRB population. The latter prediction could be comparable to results of simultaneous multiwavelength observations of individual events. Note that in this model many FRBs do not have optical counterparts, as only strong magnetar flares may have significant ion tails.

5.1.3. Soft Gamma-Ray Repeater Giant Flares as FRB Counterparts

More generally, in many FRB models, the emission processes are initiated by soft gamma-ray repeater (SGR) giant flares. The energy released by giant flares is typically specified in the γ-ray band, where the Fermi/GBM survey suggests constraints ranging between $\eta \lesssim 10^5$ (0.1 s counterparts, assuming no extant detections) and $\eta \sim 10^7$ (100 s counterparts, assuming all unclassified events are giant flares). These constraints can be used to test the hypothesis that each giant flare corresponds to an FRB.

Following Ofek (2007), the rate of giant flares in the Milky Way, which hosts four SGRs, is $\lesssim 0.002$ yr^{-1} for energies $E_{\rm SGR} > 4 \times 10^{46}$ erg (this rate is based on an analysis of extragalactic giant-flare candidates) and ~ 0.1 yr^{-1} for energies $E_{\rm SGR} > 2 \times 10^{44}$ erg (Poisson errors ignored; this rate is derived from the Milky Way alone). Ofek (2007) derives the number of SGRs in a given galaxy by comparing its core-collapse supernova rate with that of the Milky Way, which is justified given the short lifetimes (O(kyr)) of active SGRs. As the overall star formation rate is a reasonable proxy for the core-collapse supernova rate (Madau & Dickinson 2014), we can derive the (local) volumetric rate of giant flares by scaling the Milky Way rate by the ratio of the local star formation rate density ($0.015\,M_\odot$ yr^{-1} Mpc^{-3}; Madau & Dickinson 2014) and the Milky Way star formation rate ($1.9\,M_\odot$ yr^{-1}; Chomiuk & Povich 2011). For $E_{\rm SGR} > 4 \times 10^{46}$ erg and $E_{\rm SGR} > 2 \times 10^{44}$ erg, the volumetric giant-flare rates are $\lesssim 2 \times 10^4$ Gpc^{-3} yr^{-1} and $\sim 8 \times 10^5$ Gpc^{-3} yr^{-1} respectively. If each giant flare produces an FRB, these volumetric rates correspond to estimates of the FRB volumetric rates for radio-band energy releases $E_{\rm FRB} = E_{\rm SGR}/\eta$ (e.g., $E_{\rm FRB} = 4 \times 10^{39}$ erg and $E_{\rm FRB} = 2 \times 10^{37}$ erg, respectively, for $\eta = 10^7$). The volumetric rate of FRBs in the local universe inferred from the Canadian Hydrogen Intensity Mapping Experiment (CHIME) is $\sim 10^5$ Gpc^{-3} yr^{-1} (Ravi 2019), approximately above an energy threshold of 2×10^{37} erg s^{-1}.[6] Thus, contrary to previous studies (Kulkarni et al. 2014; Ravi 2019), the giant-flare rate may in fact be too high to explain the FRB rate. This result would be strengthened if the value of η is substantially lower than the conservative upper bound of 10^7 derived herein. We note, however, that all rate estimates above are subject to severe Poisson errors and that this analysis will require significant refinement before firm conclusions can be drawn.

A similar analysis can be applied to any multiwavelength event that triggers an FRB. This is of particular relevance to the "cosmic comb" model, where a regular pulsar magnetosphere is "combed" by a nearby strong plasma stream with a ram pressure higher than the magnetic pressure in the magnetosphere. The stream triggers magnetic reconnection that accelerates particles within the magnetosphere, producing coherent emission through the curvature-radiation or cyclotron instability mechanisms. On the one hand, when the plasma stream comes from nearby energetic events, such as active galactic nucleus flares, those events should be detected as FRB counterparts. On the other hand, when the stream comes from closer but less-luminous events, such as stellar flares from a companion star, no detectable counterpart would occur.

5.1.4. Curvature Radiation

Another commonly discussed coherent emission process is curvature radiation (e.g., Kumar et al. 2017; Lu & Kumar 2018). For example, Lu & Kumar (2018) propose a model where counterstreaming $e^{\pm}$ plasma inside the twisted magnetosphere of a magnetar rapidly clumps due to the two-stream instability. When magnetic reconnection occurs near the magnetar surface, these clumps are accelerated along magnetic field lines and radiate coherently. The model predicts fluence ratios of $\eta \sim 1$ in all bands, so there would be no detectable FRB counterpart.

5.1.5. Fast Optical Bursts Associated with FRBs

We compare our most constraining result from Gaia ($\eta \lesssim 10^3$, assuming nondetection and using the Gaia time resolution of 4.5 s) with predictions made by Yang et al. (2019). These authors investigate the detectability of "fast optical bursts" (FOBs) associated with FRBs in two broad cases and five specific scenarios. We convert them to the constraints on the optical-to-radio fluence ratios assuming an FRB of 1 ms duration (hollow magenta triangles in Figure 1).

Case 1: FOB formed by inverse-Compton scattering between the FRB photons and ambient electrons.
- a. FOB and FRB both formed in the pulsar magnetosphere ($10^{-7} \lesssim \eta \lesssim 10^4$, $t_{\rm FOB} \sim 1$ ms).
- b. FOB formed in a surrounding nebula and FRB near the neutron star ($\eta \lesssim 10^8$, $t_{\rm FOB} \sim$ a few $\times$ 10 s).
- c. FRB formed by synchrotron-maser mechanism and FOB formed by inverse-Compton scattering between the maser electrons and the FRB photons ($\eta \lesssim 0.38$, $t_{\rm FOB} \sim 1$ ms).

Case 2: FOB and FRB formed by the same emission mechanism.
- a. Curvature radiation by particle bunches ($\eta \lesssim 3.8 \times 10^{-5}$, $t_{\rm FOB} \sim 1$ ms).
- b. Synchrotron maser ($\eta \lesssim 3.8 \times 10^{-4}$, $t_{\rm FOB} \sim 1$ ms).

We omit case 1(c) and case 2 from Figure 1 as they are too low to compare with any existing optical telescope. Compared with our Gaia result, the upper limits predicted by cases 1(a) and 1(b) are greater by ~1 and 5 orders of magnitude, while predictions of the other three scenarios are lower by ~4, 8, and

[6] An energy of $E_{\rm FRB} \sim 2 \times 10^{37}$ erg corresponds to a 2 Jy ms burst detected by CHIME at 100 Mpc.

7 orders of magnitude, respectively. Hence, a detection of FRB counterparts by Gaia (or indeed any other optical telescope) would rule out case 1(c) and case 2, and it might be able to rule out case 1(a) if the observed fluence ratio lies between $\sim 10^4$ and 10^8.

5.1.6. How Many Multiwavelength FRB Counterparts Should Blind Surveys Detect?

Finally, we estimate the counterpart detection rate from each model (Table 3) by combining the model-predicted η with the observed FRB fluence distribution. For example, the theoretical counterpart duration at 1 MeV (2.4×10^{20} Hz) from the Metzger et al. (2019) model is ~50 ms. The shortest trigger timescales of Fermi/GBM and CGRO/BATSE above 50 ms are both 64 ms. At this timescale, the band-integrated fluence threshold is $F_{0,\mathrm{GBM}} = 2 \times 10^{18}$ Jy ms Hz (7.6×10^{17} for BATSE) and $F_{\nu,0,\mathrm{GBM}} \approx \frac{2 \times 10^{18}\ \mathrm{Jy\ ms\ Hz}}{2.4 \times 10^{20}\ \mathrm{Hz}} \approx 8.4 \times 10^{-3}$ Jy ms (3.1×10^{-3} for BATSE). The model predicts that $\eta_\nu \approx 4.1 \times 10^{-7}$ at $\nu_1 = 1$ MeV, so the expected counterpart rate above $F_{\nu,0,\ \mathrm{GBM}}$ in the GBM band would be $\tilde{R}(F_\nu) = R(\frac{F_{\nu,0,\mathrm{GBM}}}{\eta_\nu}) = R(2.1 \times 10^4\ \mathrm{Jy\ ms}) \approx 2.13 \times 10^{-5}$ sky^{-1} day^{-1} (Equations (7) and 3(c); 1.9×10^{-4} for BATSE). On average, Fermi/GBM is expected to detect one such event every $\langle n \rangle \approx (2.13 \times 10^{-5})^{-1}(\frac{4\pi}{8\ \mathrm{sr}}) \approx 7.36 \times 10^4$ days (5.3×10^3 for BATSE). By comparing $\langle n \rangle$ with the relevant survey durations n (the last two columns in Table 3), it is unlikely that Fermi/LAT, GBM, or BATSE have already detected any counterparts events or will detect one in the near future, according to the prediction of Metzger et al. (2019).

As another example, we interpolate the Metzger et al. (2019) predictions to 100 keV and conservatively assume a 1 s duration counterpart in the Swift/BAT band (and the CGRO/BATSE band) with $\eta_\nu \approx 4.1 \times 10^{-6}$. At this timescale, $F_{\nu,0,\mathrm{BAT}} \approx 4.18 \times 10^{-2}$ Jy ms, and the expected counterpart rate in that band would be $R(\frac{4.18 \times 10^{-2}\ \mathrm{Jy\ ms}}{4.1 \times 10^{-6}}) = R(10^4\ \mathrm{Jy\ ms}) \approx 10^{-4}$ sky^{-1} day^{-1} and $\langle n \rangle \approx 8.95 \times 10^4$ days. Swift/BAT is not expected to have detected any FRB counterpart based on this model, unless the counterpart duration at 100 keV is significantly shorter ($\lesssim$64 ms).

We cannot comment on the predictions from Beloborodov (2017) and Yang et al. (2019), as their models only indicate the lower limits to $\langle n \rangle$.

5.1.7. Caveat Emptor

Caution should be taken in the comparisons described above. First, our technique relies on a homogeneous FRB population distribution, and the synchrotron-maser and curvature-radiation models may not be able thus far to explain nonrepeating FRBs. Although it has been argued that all FRB sources repeat in their lifetimes (Ravi 2019), some sources are clearly more active than others, and it is not yet clear whether or not they belong to the same population groups. Second, the high-energy counterpart could be either the giant flare that initiates the FRB emission processes or the afterglow, or both, but their contributions are observationally indistinguishable. Third, it might be difficult to distinguish intrinsic emissions from propagation effects, because any dense intervening medium has different attenuation effects on different wavelengths. For example, in the model of Metzger et al. (2019), it is unclear whether the keV photons would escape from supernova ejecta shells surrounding the proposed magnetars or get absorbed by the neutral gas on the FRB timescale (Margalit et al. 2018). This ambiguity makes it difficult to constrain the model based on the nondetection of X-ray counterparts. Fourth, in this work, we only focus on surveys with cadences less than 2 minutes, but longer-duration counterparts may also be possible (e.g., Petroff et al. 2015). In this case, sensitive surveys on these longer timescales should also be considered.

A further issue is that the brightest FRB sources may in fact be missed by some of the multiwavelength surveys because of the sparsity of these FRBs on the sky. Consider the possibility that the nearest FRB sources are the brightest (Shannon et al. 2018). The nearest sources might be missed by surveys using telescopes with small FOVs that are restricted to certain portions of the sky. Our technique assumes that FRBs are uniformly distributed over the sky region scanned by a survey, which is likely true for distant FRBs but may not be true for nearby FRBs or those near the Galactic plane. Although over time the anisotropic distribution would be averaged out by successive surveys, this issue may result in erroneously low estimates of η. However, this effect is mitigated by our incorporation of a Poisson error in Step 4 in Section 2, in the case of multiwavelength nondetections. It is also not a major issue for our analysis of the surveys with cataloged unidentified detections (Fermi/GBM, MAXI), because they cover the full sky besides the Galactic plane.

5.2. Comparison to Other Observations

As is evident from Figure 1, our technique generally provides stronger constraints on η than previous observations. We consider a selection of previous observational results in turn.

Some high-energy transient surveys have been blindly searched for FRB-counterpart candidates without using knowledge of individual FRB events. Yamasaki et al. (2016) (O4 in Figure 1) performed a blind search for γ-ray flashes (duration 1–10 ms) using the 7 yr Fermi/LAT data. No event is found after removing flashes associated with known steady γ-ray sources and false events produced by the diffuse background. They found a γ-ray to radio fluence ratio of $\eta \lesssim (4.2 \sim 12) \times 10^7$ by modeling FRBs as standard candles with a power-law γ-ray spectrum and estimating the comoving FRB rate density using the nine FRBs detected by then. In comparison, our technique adopts a model-independent FRB population distribution based on a directly measurable quantity (fluence) and a significantly larger sample (~50). Using our technique, we find $\eta \lesssim 1.7 \times 10^6$ (100 ms) based on the nondetection in the 7 yr of Fermi/LAT data.

In the optical band, we estimate η from a few survey subdata sets that have been blindly searched for fast transients. Wevers et al. (2018; O8 in Figure 1) developed a method to blindly search the Gaia Photometric Science Alerts database for fast transients between tens of seconds to hours. They demonstrated the method on a trial data set that spans ~23.5 deg^2 of sky and repeatedly scanned 40–50 times. Four events produced by stellar flares are found but no unclassified event is detected. The nondetection implies a optical-to-radio-band fluence ratio of $\eta \lesssim 4 \times 10^4$ using our technique. In addition, Andreoni et al. (2020; O9 in Figure 1) specifically searched for extragalactic fast optical transients with durations down to 70 s using the Dark Energy Camera as part of the Deeper Wider Faster program. The g-band limiting magnitude of one single

exposure (20 s) is ∼23 mag (AB), the FOV is 2.52 deg^2, and the total observation time of their data set is 25.76 hr. Four events with uncertain classifications are detected, but no γ-ray signal or FRB is found within ± 1 day near these transients. Using our technique, the optical-to-radio-band fluence ratio is $\eta \lesssim 6 \times 10^4$. Finally, Richmond et al. (2020; O10 in Figure 1) find no transients with durations from 1.5 s to 11.5 s using the Tomo-e Gozen wide-field CMOS mosaic camera data (limiting magnitude $V = 15.6$) with a control time of 177,502 deg^2 s. The nondetection implies that $\eta \lesssim 10^6$ using our technique.

Most previous constraints on η are based on counterpart searches in the sky region of individual FRB events, either contemporaneous or not. We summarize them below and show some of the stronger constraints in Figure 1.

A one-second-long X-ray counterpart was detected during the recent FRB event ST 200428A from the Galactic magnetar SGR 1935+2154 (Bochenek et al. 2020; The CHIME/FRB Collaboration et al. 2020). Based on the X-ray observations of Ridnaia et al. (2020), Bochenek et al. (2020) estimated that the band-integrated fluence ratio $F_X/F_{\rm radio} \sim 3 \times 10^4$ (red star in Figure 1), about one order-of-magnitude lower than our result based on the nondetection in the blind search of Swift/BAT for a one-second-long burst in a similar energy band.

MAGIC Collaboration et al. (2018; O6 in Figure 1) conducted simultaneous observations of the repeating FRB 121102 using the Arecibo telescope and MAGIC (100 GeV–50 TeV and the optical band). Five FRBs were detected during this time (mean fluence ∼2 Jy ms), but no simultaneous or persistent counterparts were found by MAGIC. This implies that $F_{>100\,\rm GeV}/F_{\rm Arecibo} \lesssim 2 \times 10^7$ for a 10 ms counterpart and $F_{\rm optical}/F_{\rm Arecibo} \lesssim 4 \times 10^3$ for a 1 ms counterpart.

Casentini et al. (2020; O5 in Figure 1) searched the AGILE archival data for MeV–GeV counterparts of two repeating FRB sources. They find no prompt emission and estimate a band-integrated fluence ratio of $F_{\rm MeV}/F_{\rm Radio} \lesssim 10^8$, assuming millisecond-scale emissions in the MeV band.

Cunningham et al. (2019) found no prompt high-energy counterparts with durations between 0.1 and 100 s for a sample of 23 FRBs in the Fermi/GBM, Fermi/LAT, and Swift data. They estimate the fluence ratio to be $\eta \lesssim 10^{7-12}$ for the timescale of 0.1 s (and $\eta \lesssim 10^{8-13}$ for 100 s).

Anumarlapudi et al. (2020; O3 in Figure 1) find no prompt X-ray counterparts for a sample of 42 FRBs in the AstroSat/CZTI data (20–200 keV) and estimate the fluence ratio to be $F_{\rm X}/F_{\rm Radio} \lesssim 10^{8-10}$.

Scholz et al. (2017; O1 and O2 in Figure 1) present simultaneous observations of the repeating FRB 121102 using the XMM-Newton, Chandra, and Fermi/GBM telescopes along with several radio telescopes. They found 12 radio bursts and no contemporaneous counterpart emission. They estimate that $\eta \lesssim 4 \times 10^8$ in the Fermi/GBM band and $\eta \lesssim 3 \times 10^6$ in the X-ray band (0.5–10 keV) assuming bursts of <700 ms. In addition, they find no X-ray counterparts in the sky region at any time during these observations. Using the fluence distribution of radio bursts from FRB 121102, they estimate that $\eta \lesssim 5 \times 10^7$ in the XMM-Newton band (0.1–15 keV) and $\eta \lesssim 10^8$ in the Chandra band (0.5–7 keV), assuming 5 ms X-ray bursts.

Hardy et al. (2017; O7 in Figure 1) conducted simultaneous observations of FRB 121102 using the high-speed optical camera ULTRASPEC on the Thai National Telescope and the Effelsberg radio telescope. They detected 13 radio events and no prompt optical counterparts. They compared the median radio fluence of those bursts with the optical detection limit and find $F_{\nu,767\,\rm nm}/F_{\nu,1.4\,\rm GHz} \lesssim 0.077$, corresponding to a band-integrated fluence ratio of $\eta \lesssim 2 \times 10^4$.

Finally, in a class of FRB models, the emission processes are initiated by SGR giant flares. Tendulkar et al. (2016) estimate that $F_{\nu,1.4\,\rm GHz}/F_\gamma \lesssim 10^7$ Jy ms erg^{-1} cm^2 for a 10 ms radio fluence based on the radio nondetection of a γ-ray giant flare from the magnetar SGR 1806–20. Their results imply $\eta = F_\gamma/F_{\rm radio} \gtrsim 10^{10}$, which is inconsistent with our γ-ray upper limits and thus in tension with the idea that SGR flares generally produce FRBs. This outcome is consistent with the discussion in Section 5.1.3.

5.3. Future Searching Strategies

In the absence of FRB-counterpart detections, η can be constrained from either simultaneous multiwavelength and radio searches or blind searches combined with the FRB population (considered in this paper). The observational strategies are slightly different in these two cases, given the nature of the FRB fluence distribution.

First, we emphasize that simultaneous radio and multi-wavelength searches are only worthwhile if they probe to lower values of η than existing blind multiwavelength searches. In a simultaneous counterpart search with a nondetection, the upper limit to $\eta \propto f_0 \cdot \Delta t$. Here, Δt is the timescale and f_0 is the corresponding detection flux threshold. The FOV (Ω) makes no difference. The total observation duration (L) is also irrelevant, until the next FRB occurs.

In contrast, in a blind search where no counterpart is found, the upper limit on η also depends on L and Ω. The counterpart rate upper bound $R \propto L^{-1} \cdot \Omega^{-1}$ (step 4 in Section 2). Using the broken-power-law fluence distribution, the radio fluence threshold that would have produced the same rate R is $F_{\nu,0,\rm Radio} \propto R^{1/\alpha} \propto L^{-1/\alpha} \cdot \Omega^{-1/\alpha}$. Meanwhile, the fluence threshold in the band of the counterpart is $F_{\nu,0,\rm Band} \propto f_0 \cdot \Delta t$. Therefore,

$$\begin{aligned} \eta &\propto f_0 \cdot \Delta t \cdot \Omega^{1/\alpha} \cdot L^{1/\alpha}, \\ &\propto 10^{-0.4\,m} \cdot \Delta t \cdot \Omega^{1/\alpha} \cdot L^{1/\alpha}. \end{aligned} \tag{11}$$

Here, m is the absolute magnitude and α is the power-law index of the fluence distribution (Equation (3)). Assuming nondetection or a low counterpart detection rate, the power-law index of the ASKAP FRB sample ($\alpha_2 = -2.2$) is more relevant than that of Parkes ($\alpha_1 = -1.18$), because the former describes events with rate below $R_b \approx 170$ sky^{-1} day^{-1} (Equation 3(c)) and the latter describes more common events (Equation 3(b)). Using α_2, $\eta \propto f_0 \cdot \Delta t \cdot \Omega^{-0.45} \cdot L^{-0.45}$, so one could enhance the constraint on η by one order of magnitude by lowering the detection flux threshold by 10 times, using a 10 times shorter timescale, or increasing the FOV or survey duration by 158 times (15 times if using α_1).

Nonetheless, there may be reasons to also require large FOVs or survey areas. If counterpart events are rare in the local universe, a significant number of nearby galaxies would need to be included in a blind search.

6. Conclusions

We have developed and demonstrated a technique to estimate η—the ratio between the energy emitted by the multiwavelength counterparts of FRBs and FRBs themselves—by combining existing multiwavelength fast transient surveys with the fluence distribution of the FRB population. The extremely large FOVs and observation durations of surveys from the optical to the TeV bands, combined with the high all-sky rate of FRBs, mean that the locations of several FRBs undetected by radio telescopes have likely been observed by telescopes across the electromagnetic spectrum. We use the properties of several multiwavelength surveys (listed in Table 1) to constrain η under the assumption that no FRB counterparts have been detected and, in some cases, to estimate η under the assumption that all unclassified transient events are FRB counterparts (Table 2 and Figure 1). We conclude the following:

1. Even our most conservative constraints/estimates for η are lower than several existing results, which are largely based on targeted observations of known FRB locations, coordinated between multiple telescopes.
2. The FRB models proposed by Metzger et al. (2019) and Beloborodov (2019), which involve synchrotron masers initiated by shocks driven by young-magnetar flares, are closest to our constraints on η. In some scenarios, Gaia should have already detected several FRB counterparts. FRB counterparts may be found among unclassified transient events. This demonstrates the power of our technique to address FRB model predictions. However, in the high-energy bands, surveys by the Fermi and Swift satellites are not likely to have detected FRB counterparts unless the photon indices are significantly steeper than -2.
3. Our technique can also be used to test predictions for multiwavelength emission that is associated with but not directly caused by FRBs. For example, we find evidence that the volumetric rate of magnetar giant flares that emit a factor of $\eta = 10^7$ larger energies in γ-rays than FRBs do in the radio band is over an order of magnitude higher than the FRB volumetric rate (Section 5.1.3).
4. The apparent rarity of multiwavelength FRB counterparts, and correspondingly likely low values of η, implies that future multiwavelength surveys are likely to only detect counterparts to the brightest FRBs. Given the steepness of the FRB fluence distribution at the bright end (James et al. 2019), future blind surveys searching for FRB counterparts should prioritize sensitivity, and the ability to probe appropriately short timescales, over FOV and survey duration.

Although our results are robust to uncertainties in the FRB fluence distribution, the future application of our technique to better constrain FRB models will require a careful analysis of unclassified transient events in existing survey data sets. In addition, we assume a homogeneous population of FRB sources, which may not be the case, and it is also possible that some (e.g., soft X-ray, or blue optical) FRB counterparts are absorbed or scattered in dense surrounding media. Multi-wavelength observations of nearby individual sources (e.g., Casentini et al. 2020; Pilia et al. 2020; Tavani et al. 2020) are a complementary means to address the nature of the FRB engine and emission mechanism.

We thank Sterl Phinney and Casey Law for useful discussions. This material is based upon work supported by the National Science Foundation under grant No. AST-1836018. W.L. is supported by the David and Ellen Lee Fellowship at Caltech.

ORCID iDs

Ge Chen https://orcid.org/0000-0003-2867-4544
Vikram Ravi https://orcid.org/0000-0002-7252-5485
Wenbin Lu https://orcid.org/0000-0002-1568-7461

References

Aleksić, J., Ansoldi, S., Antonelli, L. A., et al. 2016, APh, 72, 76
Andreoni, I., Cooke, J., Webb, S., et al. 2020, MNRAS, 491, 5852
Anumarlapudi, A., Bhalerao, V., Tendulkar, S. P., & Balasubramanian, A. 2020, ApJ, 888, 40
Atwood, W. B., Abdo, A. A., Ackermann, M., et al. 2009, ApJ, 697, 1071
Bannister, K. W., Deller, A. T., Phillips, C., et al. 2019, Sci, 365, 565
Barthelmy, S. D., Barbier, L. M., Cummings, J. R., et al. 2005, SSRv, 120, 143
Beloborodov, A. M. 2017, ApJL, 843, L26
Beloborodov, A. M. 2019, arXiv:1908.07743
Bessell, M. S., Castelli, F., & Plez, B. 1998, A&A, 333, 231
Bhandari, S., Keane, E. F., Barr, E. D., et al. 2018, MNRAS, 475, 1427
Biryukov, A., Beskin, G., Karpov, S., et al. 2015, BaltA, 24, 100
Bochenek, C. D., Ravi, V., Belov, K. V., et al. 2020, arXiv:2005.10828
Casentini, C., Verrecchia, F., Tavani, M., et al. 2020, ApJL, 890, L32
Chatterjee, S., Law, C. J., Wharton, R. S., et al. 2017, Natur, 541, 58
CHIME/FRB Collaboration, Amiri, M., Bandura, K., et al. 2019a, Natur, 566, 235
CHIME/FRB Collaboration, Andersen, B. C., Bandura, K., et al. 2019b, ApJL, 885, L24
Chomiuk, L., & Povich, M. S. 2011, AJ, 142, 197
Cordes, J. M., & Wasserman, I. 2016, MNRAS, 457, 232
Cunningham, V., Cenko, S. B., Burns, E., et al. 2019, ApJ, 879, 40
Cwiek, A., Mankiewicz, L., Batsch, T., et al. 2014, Proc. SPIE, 9290, 92900T
Fonseca, E., Andersen, B. C., Bhardwaj, M., et al. 2020, ApJ, 891, L6
Frei, Z., & Gunn, J. E. 1994, AJ, 108, 1476
Fukugita, M., Ichikawa, T., Gunn, J. E., et al. 1996, AJ, 111, 1748
Gehrels, N. 1986, ApJ, 303, 336
Gehrels, N. 1997, NCimB, 112B, 11
Ghisellini, G. 2017, MNRAS, 465, L30
Hardy, L. K., Dhillon, V. S., Spitler, L. G., et al. 2017, MNRAS, 472, 2800
Hoshino, M., & Arons, J. 1991, PhFlB, 3, 818
James, C. W., Ekers, R. D., Macquart, J. P., Bannister, K. W., & Shannon, R. M. 2019, MNRAS, 483, 1342
Keane, E. F., & Petroff, E. 2015, MNRAS, 447, 2852
Kulkarni, S. R., Ofek, E. O., Neill, J. D., Zheng, Z., & Juric, M. 2014, ApJ, 797, 70
Kumar, P., Lu, W., & Bhattacharya, M. 2017, MNRAS, 468, 2726
Kumar, P., Shannon, R. M., Osłowski, S., et al. 2019, ApJL, 887, L30
Langdon, A. B., Arons, J., & Max, C. E. 1988, PhRvL, 61, 779
Law, C. J., Abruzzo, M. W., Bassa, C. G., et al. 2017, ApJ, 850, 76
Law, N. M., Fors, O., Ratzloff, J., et al. 2015, PASP, 127, 234
Law, N. M., Kulkarni, S. R., Dekany, R. G., et al. 2009, PASP, 121, 1395
Long, K., & Pe'er, A. 2018, ApJL, 864, L12
Lu, W., & Kumar, P. 2018, MNRAS, 477, 2470
Lyubarsky, Y. 2014, MNRAS, 442, L9
Lyubarsky, Y. 2020, arXiv:2001.02007
Macquart, J. P., & Ekers, R. 2018, MNRAS, 480, 4211
Madau, P., & Dickinson, M. 2014, ARA&A, 52, 415
MAGIC Collaboration, Acciari, V. A., Ansoldi, S., et al. 2018, MNRAS, 481, 2479
Mankiewicz, L., Batsch, T., Castro-Tirado, A., et al. 2014, RMxAC, 45, 7
Marcote, B., Nimmo, K., Hessels, J. W. T., et al. 2020, Natur, 577, 190
Margalit, B., Metzger, B. D., Berger, E., et al. 2018, MNRAS, 481, 2407
Margalit, B., Metzger, B. D., & Sironi, L. 2020, MNRAS, 494, 4627
Matsuoka, M., Kawasaki, K., Ueno, S., et al. 2009, PASJ, 61, 999
Meegan, C., Lichti, G., Bhat, P. N., et al. 2009, ApJ, 702, 791
Melrose, D. B. 2017, RvMPP, 1, 5
Metzger, B. D., Margalit, B., & Sironi, L. 2019, MNRAS, 485, 4091
Ofek, E. O. 2007, ApJ, 659, 339
Petroff, E., Bailes, M., Barr, E. D., et al. 2015, MNRAS, 447, 246
Petroff, E., Barr, E. D., Jameson, A., et al. 2016, PASA, 33, e045

Pilia, M., Burgay, M., Possenti, A., et al. 2020, arXiv:2003.12748
Preece, R. D., Briggs, M. S., Mallozzi, R. S., et al. 1998, ApJL, 506, L23
Prochaska, J. X., Macquart, J.-P., McQuinn, M., et al. 2019, Sci, 366, 231
Prusti, T., de Bruijne, J., Brown, A. G., et al. 2016, A&A, 595, A1
Ravi, V. 2019, NatAs, 3, 928
Ravi, V., Catha, M., D'Addario, L., et al. 2019, Natur, 572, 352
Richmond, M. W., Tanaka, M., Morokuma, T., et al. 2020, PASJ, 72, 3
Ridnaia, A., Svinkin, D., Frederiks, D., et al. 2020, arXiv:2005.11178
Scholz, P., Bogdanov, S., Hessels, J. W. T., et al. 2017, ApJ, 846, 80
Shannon, R. M., Macquart, J. P., Bannister, K. W., et al. 2018, Natur, 562, 386
Spitler, L. G., Scholz, P., Hessels, J. W. T., et al. 2016, Natur, 531, 202
Tavani, M., Verrecchia, F., Casentini, C., et al. 2020, ApJ, 893, L42
Tendulkar, S. P., Kaspi, V. M., & Patel, C. 2016, ApJ, 827, 59
The CHIME/FRB Collaboration, Andersen, B. C., Bandura, K. M., et al. 2020, arXiv:2005.10324
Vedantham, H. K., Ravi, V., Mooley, K., et al. 2016, ApJL, 824, L9
Waxman, E. 2017, ApJ, 842, 34
Wevers, T., Jonker, P. G., Hodgkin, S. T., et al. 2018, MNRAS, 473, 3854
Yamasaki, S., Totani, T., & Kawanaka, N. 2016, MNRAS, 460, 2875
Yang, Y.-P., Zhang, B., & Wei, J.-Y. 2019, ApJ, 878, 89
Zhang, B. 2017, ApJL, 836, L32